WALL PRESSURE SIGNATURE OF SEPARATED FLOWS: A COMPARISON BETWEEN FLAT PLATE AND AIRFOIL

Arnaud Le Floc'h, Alexandre Suryadi, Nan Hu, Michaela Herr
Department of Wind Energy
Institut für Aerodynamik und Strömungstechnik
Deutsches Zentrum für Luft- und Raumfahrt (DLR)
38108 Braunschweig, Germany
arnaud.lefloch@dlr.de,alexandre.suryadi@dlr.de,
nan.hu@dlr.de,michaela.herr@dlr.de

Sen Wang, Sina Ghaemi
Laboratory of Turbulent Flows
Mechanical Engineering Department
University of Alberta
Edmonton, AB T6G 2H5, Canada
sen6@ualberta.ca,ghaemi@ualberta.ca

Jérôme Vétel
Laboratoire de dynamique des fluides
Département de génie mécanique
Polytechnique Montréal
Montréal, QC H3T 1J4, Canada
jerome.vetel@polymtl.ca

Giuseppe Di Labbio, Louis Dufresne
Laboratoire de thermofluide pour le transport
Département de génie mécanique
École de technologie supérieure
Montréal, QC H3C 1K3, Canada
giuseppe.dilabbio@etsmtl.ca, louis.dufresne@etsmtl.ca

INTRODUCTION

In both internal and external aerodynamics, pressure induced separation bubbles can be formed for instance near the trailing edge of an airfoil. Specifically, in wind energy, one of the environmental restrictions is the proximity of wind parks to residential areas. Consequently, maintaining wind turbine performance and reliability as well as complying with noise regulations are important challenges. Poor design considerations, imprecise operational monitoring and incomplete knowledge of the physics of flow separation all contribute to boundary layer separation from wind turbine blade surfaces, reducing efficiency and amplifying noise emission (Suryadi & Herr, 2015; Suryadi, 2019). Facing on-site adverse environmental conditions, tracking flow separation on wind turbine blades is essential not only for aerodynamics but also for acoustics. The first step is to better understand the physics of separated flows and the mechanisms driving the wall pressure fluctuations, p_w, beneath a separating turbulent boundary layer.

In this study we aim to derive the flow separation topology from wall pressure measurements for the DU96-W-180 airfoil investigated experimentally in the Acoustic Wind Tunnel Braunschweig (AWB) at DLR. One of the underlying questions is how to recognize the flow separation signature in wall pressure and whether it is a weak separation causing a mild noise increase, or a larger separation causing a significant one. To answer this question, the merging of different databases appears necessary considering that previous measurements on wind turbine blades did not include velocity measurements (e.g., PIV) or shear stress sensors (Suryadi & Herr, 2015). Assuming that the same flow physics produces the same results in both configurations, similar phenomena should take place either near the trailing edge of an airfoil at a high angle of attack or on a flat plate with an imposed APG. In this paper, we present time and frequency domain parameters that characterize the onset and development of flow separation from three databases including a flat plate and two airfoils.

MERGING DATABASES

Three databases dealing with APG-induced flow separation are available for the present study. (1) The wall pressure and velocity fields of a family of turbulent separation bubbles (TSBs) was recently measured using 2D-2C PIV in the boundary layer wind tunnel of ÉTS Montréal (Le Floc'h, 2021). Three distinct TSBs were investigated at $Re_\theta = 5000$: (a) a large TSB with a 41-cm-long recirculation region; (b) a medium 11-cm-long TSB; (c) a small TSB with no backflow. (2) In investigating flow separation noise, the wall pressure of the DU96-W-180 was measured in the AWB (Suryadi & Herr, 2015). The airfoil was set to pre-stall angles of attack from $-0.8°$ to $10.2°$, where at the largest angle, massive flow separation was observed from oil film visualizations. (3) The time resolved topology of a trailing edge TSB was recently analyzed on a NACA 4418 airfoil, where modal decomposition illustrated the unsteady topology of the recirculation region, including a low frequency oscillation of the separation line, commonly referred to as the *breathing* motion (Ma *et al.*, 2020; Wang & Ghaemi, 2022). Such unsteadiness is very similar to that observed on the flat plate where both separation and reattachment lines exhibit large oscillations (Le Floc'h, 2021).

In Fig. 1, the mean flow topologies are presented for each database. On the left side, the contours of the mean streamwise velocity field for both the large flat-plate TSB (top) and the NACA 4418 (bottom) indicate two massively separated regions with visible differences. The large TSB appears somewhat symmetric thanks to the combination of APG and FPG effects, whereas the TSB formed on the trailing edge of the NACA 4418 is clearly tilted in the direction of the wake formed downstream of the profile. With an angle of attack of $9.7°$, Wang & Ghaemi (2022) obtained a recirculation region on the last 20% of the chord, which resembles closely the DU96-W-180 case for $\alpha = 7.8°$. In the oil film visualizations from Fig. 1, the solid green lines define the separation line where the two recirculation regions downstream span ap-
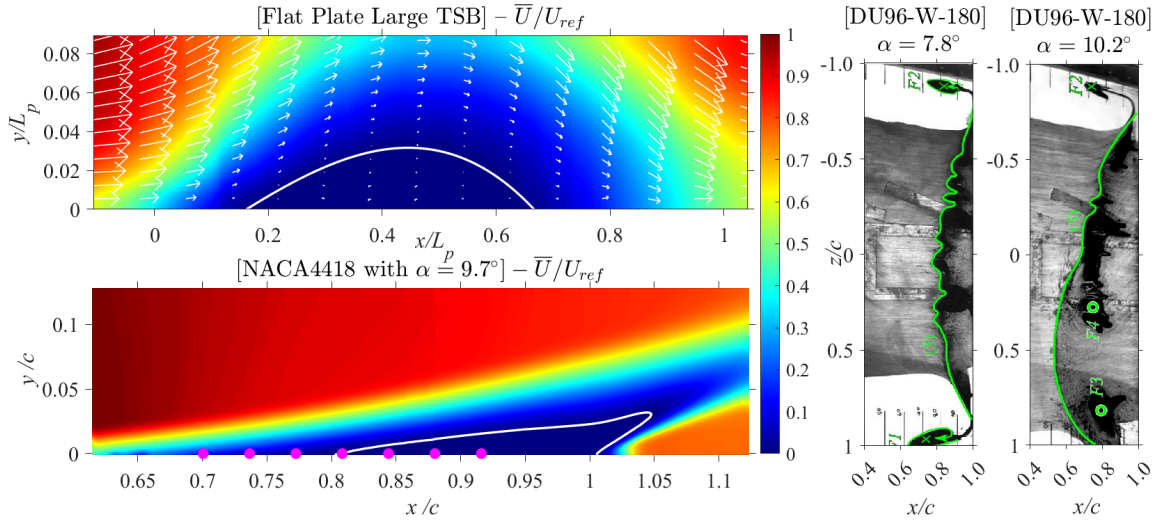
Figure 1: Top left: isocontours of the mean streamwise velocity component $\overline{U}/U_{ref}$ in the large flat plate TSB from Mohammed-Taifour & Weiss (2016) and Le Floc'h *et al.* (2020). The white arrows indicate mean velocity from center span. The white solid line represents $\overline{U}/U_{ref} = 0$ m/s. Bottom left: isocontours of mean streamwise velocity $\overline{U}/U_{ref}$ from Wang & Ghaemi (2022). Flow goes from left to right and the magenta dots indicate the 7 microphone locations. Right side: two oil film visualizations from the DU96-W-180 airfoil for two angles of attack ($\alpha = 7.8°$ and $10.2°$). Green solid line is representative of the mean separation line and foci F1 to F4 are identified.

proximately 20% and 40% of the chord for $\alpha = 7.8°$ and $10.2°$ respectively. Even if the case at $10.2°$ appears asymmetric, the classical topological combination of saddle point flanked by two foci is still apparent. In what follows, we examine and compare the wall pressure signatures of the three databases.

SPECTRAL ANALYSIS OF WALL PRESSURE
Comparing Separated Flow Spectra

The first section deals with the spectral response of separated flows. A summary of the experimental setup of the different geometries being considered is presented in Table 1. The interest of this comparison is to extract common physical features of separated flows despite the limitations of wall pressure measurements associated with each case (cf. Table 2). The flat-plate wall-pressure measurements were performed using a series of Meggitt 8507C-1 sensors, each attached to a 27-mm-long tube with 0.8 mm diameter where the associated resonance frequency limited the maximum sampling rate at $f_s = 2$ kHz. Flush-mounted measurements at $f_s = 16$ kHz were also performed in Le Floc'h *et al.* (2020) that confirmed the expected levels of turbulent fluctuations near the separated region. Similar observations were made for the NACA 4418 measurements, using B&K 4964 microphones, regarding the Helmholtz resonance due to the presence of a cavity behind the pinhole that connected to the wing surface. This feature limited the upper range of the spectral response to $\simeq 460$ Hz. On the other side of the spectrum, the Kulite ultra-miniature pressure transducers on the DU96-W-180 were further processed with a high-pass filter using a cut-off frequency of 200 Hz, making the low-frequency analysis for the DU96-W-180 airfoil impractical.

The power spectral densities (PSDs) for the three datasets are shown in one figure, Fig. 2, where the frequency axis is normalized using the Strouhal number: $St_L = fL_b/U_{ref}$ as L_b is the mean separation length and U_{ref} is the nominal inlet velocity. Note that oil film visualizations only yield a rough estimate of the separation length for the DU96-W-180 compared to PIV data for the two other geometries. Three ranges of frequencies are also highlighted: in yellow the low-frequency

Table 1: Flow parameters for each database.

Geometry	Flat plate	DU96-W-180	NACA 4418
U_{ref} (m/s)	25	40, 50, 60	10.2
α, (°)	—	−0.8 - 10.2	9.7
δ_{ZPG} (mm)	29.8	—	17.8
δ_{TE} (mm)	—	12 - 39	88
Length scale (m)	3	0.30	0.975

Table 2: Wall pressure sensors.

Sensor	Meggitt	Kulite	Brüel & Kjær
Type	8507C-1	LQ-062-0.35BarA	4964
f_s (Hz)	2 000	100 000	20 000
T_{acq} (s)	300	30	60
$\varnothing$ (mm)	0.8	0.5	0.5

breathing motion ($St_L < 0.15$), in red the medium-frequency vortex shedding ($St_L \in [0.2 - 2]$) and finally in green the high-frequencies ($St_L > 3$) including small scales from turbulence. Comparing the streamwise positions of incipient detachment (ID, defined by a forward flow fraction of $\gamma = 99\%$), mean or transitory detachment (TD, defined by $\gamma = 50\%$) and inside the recirculation ($\gamma \simeq 20\%$), a typical spectrum shows a peak first in the high frequency range at the onset of separation and moves towards a peak at about $St_L \simeq 0.3 - 0.5$ inside the recirculation for all three configurations. However, as expected, the DU96-W-180 results do not show any extent in the breathing range but both the NACA 4418 and the flat plate TSB feature a strong activity at the onset of separation (near the ID point), notably for the blue curves of the large TSB.

Regarding the mid to high St_L section of the spectrum, Fig. 2b presents an interesting feature where the slope of the PSD at the end of the vortex shedding range (red background) appears to be deflected for points located inside the recirculation region at $St_L > 2$. The subsequent slope in the high-frequency region (green background) convincingly decreases for the DU96-W-180 and the flat plate. This is also observed
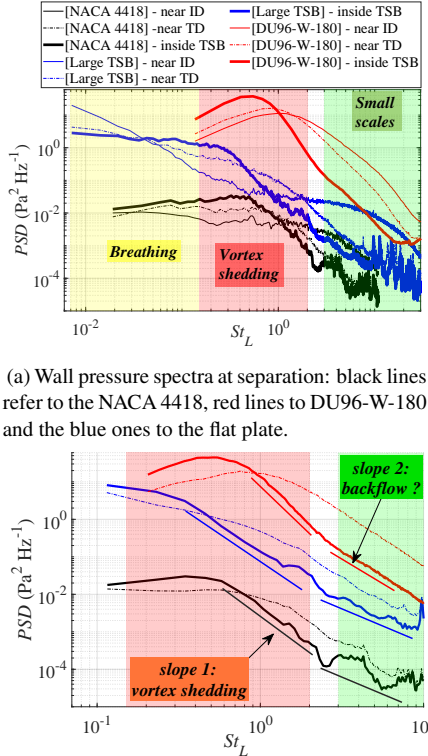
(a) Wall pressure spectra at separation: black lines refer to the NACA 4418, red lines to DU96-W-180 and the blue ones to the flat plate.

(b) Same legend as 2a. PSDs computed with reduced windows and multiplied by 30 for DU96-W-180 to ease the view.

Figure 2: Power spectral densities of p_w for the three databases, upstream and downstream of separation.

for the NACA 4418, though it is less pronounced. Such a feature is not observed upstream or near TD, which suggests that this spectral deviation in this high frequency range could be linked to the recirculation activity and therefore serve as a criterion for the existence of flow separation.

Tracking Flow Separation at High Frequencies

Beyond single point measurements, we pursue the investigation of backflow motion using the convection information between two close enough neighboring pressure sensors. The classical signature obtained is that two-point cross-correlations exhibit a downstream motion associated with the roll-up and shedding of vortical structures from the shear layer that corresponds to the global peak in the medium-frequency range. As we are searching for a possible higher-frequency motion, we compare instead the phase angle computed from the cross-PSD. The assumption here is that if we were to observe backflow, the slope of the CPSD phase angle $\theta(f)$ should have its sign flipped from positive to negative, following the relation: $d\theta/df = 2\pi\Delta_x/U_c$, with Δ_x the distance between the two sensors (Bendat & Piersol, 2011). On top of Fig. 3, we present the PSDs of the DU96-W-180 for two streamwise locations, one upstream ($x/c = 0.81$) and one downstream ($x/c = 0.95$) of separation, at $\alpha = 7.8°$ for various reference velocities. Remarkably, the pairs of points behave consistently as the slope deviation between mid- and high-frequencies is only observed for the downstream point inside the recirculation, but not upstream. At the bottom of Fig. 3, we then look at the phase evolution between the downstream point at $x/c = 0.95$ and its immediate upstream neighbor at $x/c = 0.94$. For the frequency range corresponding to the vortex shedding, the phase

has a positive slope, indicating that $d\theta/df = 2\pi\Delta_x/U_c > 0$. At higher frequencies, the phase evolution in all three cases shows a downward trend that started with the PSD bifurcation, as materialized by the vertical dash lines in Fig. 3.
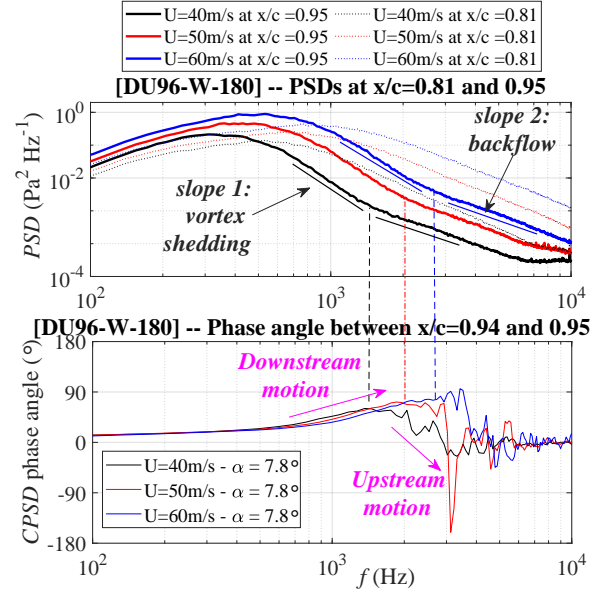

Figure 3: DU96 PSDs upstream and downstream of separation at different referent velocities for the case $\alpha = 7.8°$. Bottom: Phase angle between two close sensors inside the recirculation.
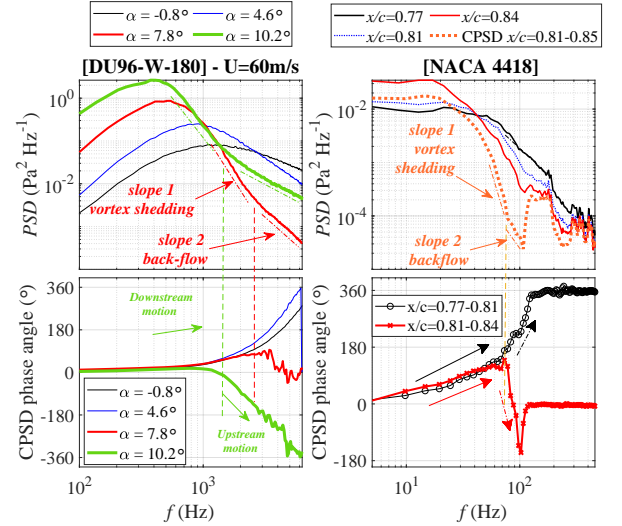

Figure 4: Wall-pressure spectra near separation. Left: DU96-W-180 at $U = 60$ m/s and various α, right: NACA 4418

This feature is of particular interest and demonstrates that a single pair of pressure transducers can detect both a mid-frequency downstream motion and a higher-frequency upstream motion linked to flow recirculation. To the best of the authors' knowledge, this has not been documented in the literature. This phenomenon is further examined with the comparison of the two airfoils side by side in Fig. 4. Spectra for the DU96-W-180 profile are plotted for a point inside the re-

3

circulation located at $x/c = 0.95$ while considering one reference velocity ($U = 60$ m/s) and various angles of attack ($\alpha = [-0.8°, 4.6°, 7.8°, 10.2°]$). This method allows a better illustration of the progressive increase in the amount of backflow development near the trailing edge. The first two angles (cf. black and blue curves at $\alpha = -0.8°$ and 4.8, respectively on the left side of Fig. 4) correspond to attached cases as confirmed with oil films (not shown here for brevity). Moreover, these spectra show no particular deviation or bifurcation up to $f = 6$ kHz. The phase angle computed from the same aforementioned pair of sensors ($x/c = 0.94 - 0.95$) revealed a uniform downstream motion that decelerates when increasing α (blue curve at 4.6° for the phase shows a greater slope than the black one at $-0.8°$).

In contrast with attached cases, the largest two angles of attack present the same feature of reversed slope for the CPSD phase angle as in Fig. 3, that takes place around $\simeq 2.5$ kHz for $\alpha = 7.8°$ and $\simeq 1.5$ kHz for $\alpha = 10.2°$, which can be interpreted as increased amount of recirculating structures. A noteworthy observation can be made for the NACA 4418 that ended up presenting the same phase angle signature. Indeed, at $f = 80$ Hz ($St_L \simeq 2$) near the end of the vortex shedding range, two pairs of neighboring microphones $P3 - P4$ ($x/c = 0.77 - 0.81$) and $P4 - P5$ ($x/c = 0.81 - 0.84$) are used to compute the convection information between regions upstream and downstream of separation (located at $x/c = 0.81$). Consistent with the DU96-W-180 results, the NACA 4418 exhibits a reversed phase angle slope from $f = 80$ Hz that coincides with the spectral bifurcation for both the PSD of the microphone inside the TSB (P5 at $x/c = 0.84$) and the cross-PSD (P4-P5). Note that the distance between the two sensors in the NACA database is roughly 35 mm apart ($\simeq 0.39\delta_{TE}$) versus 3 mm apart ($\simeq 0.125\delta_{TE}$) for DU96-W-180 database, as the effect of the Reynolds number likely influences the maximum distance available between two sensors without losing the convection information.

Therefore, we conclude the spectral analysis with the fact that the low-frequency breathing motion (Le Floc'h *et al.*, 2020; Wang & Ghaemi, 2022) of a TSB is not the only metric that can inform on the amplitude of separation. As it turns out, the recirculation motion can also be detected at the other end of the spectrum, just above the frequency range of the vortex shedding.

TIME DOMAIN ANALYSIS OF WALL PRESSURE

In this section, we now turn our attention to the time domain. Skewness and kurtosis are the two most popular criteria used to quantify probability density functions for wall pressure measurements. Skewness is typically a measure of the asymmetry of a probability density function, namely, if the positive pressure side has a longer tail, the skewness will be positive and vice versa. In the following sections, we first focus on the canonical configuration of the flat plate for three distinct levels of separation (Le Floc'h *et al.*, 2020) to distinguish the *attached* case versus the *separated* case in a time-averaged sense.

Distinct Thresholds of Separation on a Flat Plate

Following Le Floc'h (2021)'s investigation of three distinct geometries that yielded different amplitudes of flow separation, we now aim to investigate the effect of an APG leading to either a massive, weak or even absent amount of mean backflow occurring further downstream.
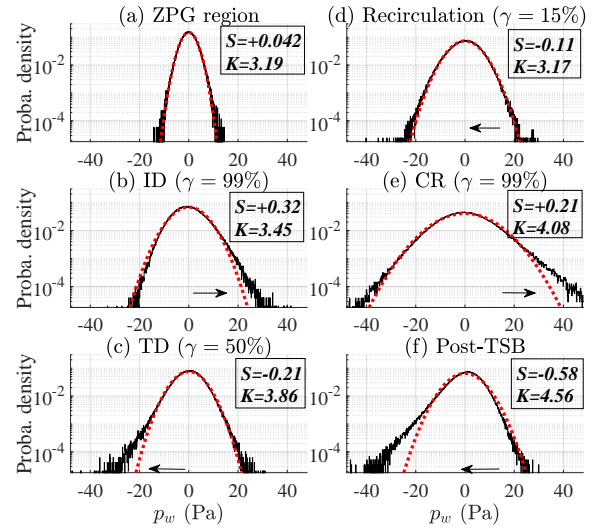

Figure 5: Probability densities for p_w from the large TSB at six different locations in black: (a) ZPG region, (b) incipient detachment, (c) mean detachment (TD), (d) near maximum of recirculation, (e) complete reattachment and (f) post-TSB region. Red dashed curves correspond to a fitted normal distribution.

Probability densities of p_w are shown in Fig. 5 for six locations of interest: first in the ZPG region, at the onset of separation (ID), the mean separation region (TD), inside the recirculation, at complete reattachment (CR) and finally far downstream of the bubble. Note that the abscissa are not normalized by the standard deviation to better evaluate the amplitude changes. The ZPG region is characterized by relatively small high-amplitude pressure peaks (noted HAPPs), with slightly positive skewness of $S = 0.042$ that is close to Naka *et al.* (2015); Gibeau & Ghaemi (2021). The onset of separation is marked by a significant amplification of positively skewed HAPP events: Fig. 5(b) corresponds to the ID point, where the low-frequency breathing is best observed using p_w (Mohammed-Taifour & Weiss, 2016) and leads to $S = +0.32$. The regions of mean separation and inside the TSB are marked by negatively skewed HAPP events. This change has also been documented in a different pressure-induced separation behind an axisymmetric bump (Byun & Simpson, 2010). The latter linked these positive HAPP events upstream of mean separation to large eddies provoking large zones of negative velocity away from the wall and then added that the switch to negative HAPPs in the recirculation was then likely due to the low-pressure vortical structures from the outer layer. The amplitude of p_w becomes maximum at complete reattachment shown in Fig. 5(e). This location also corresponds to the absolute maximum of $c_{p'}$ (Le Floc'h *et al.*, 2020). It is associated with strong positive HAPP events ($S = +0.21$) until it becomes negative again far downstream of the TSB. These results are consistent with what Sasaki & Kiya (1985) had observed at the reattachment region over a blunt plate who associated these positive HAPP events at reattachment with the inrush of irrotational fluid of high total pressure impinging on the wall as the shear layer reattaches.

To better distinguish between scales, we now focus on the skewness and kurtosis distributions for the small, medium and large TSBs. Figs. 6 and 7 present the results from raw data (left ordinate, black curves), compared to the equivalent high-order moment contributions from filtered fluctuations (right ordinate, red curves). The low-, band- and high-pass filtering

aim to cover the ranges of the breathing motion ($St_L < 0.15$), the vortex shedding ($0.15 < St_L < 2$) and the small scales ($St_L > 3$), respectively. Instead of computing a new skewness/kurtosis value for filtered traces, we compute a different moment ratio, $\text{Moment}_i(p_{w, \, filtered})$, which is related to the original high-order moment, $\text{Moment}_i(p_{w, \, original})$, shown in Eq. 1:

$$\text{Moment}_i(p_{w, \, original}) = \frac{\overline{(p_w)^i_{original}}}{\sigma^i_{(p_w)_{original}}}, \text{ with i } = 3, 4$$

$$\text{Moment}_i(p_{w, \, filtered}) = \frac{\overline{(p_w)^i_{filtered}}}{\sigma^i_{(p_w)_{original}}}, \text{ with i } = 3, 4 \tag{1}$$

where $\text{Moment}_{i=3,4}$ correspond to the skewness (Sk) and kurtosis (Ku), respectively. The denominators are the same non-filtered standard deviation $\sigma_{(p_w)_{original}}$ for all the cases. The reason is that the standard deviation of low-pass signals in the ZPG region are typically small, provoking abnormally large skewness values in low-pass results even though there is no such activity observed in that zone. With this approach, we aim to discuss the contribution from each frequency range to possible peaks in the statistical moments of p_w.

Of particular interest, we note that the APG first causes a positive peak in skewness and a peak with leptokurtic ($K > 3$) indicating an intermittent large amplitude for both attached and separated cases. Separated TSBs in a mean sense (large and medium) show a subsequent negative skewness inside the recirculation, whereas the small TSB (analogous to an APG TBL) remains positively skewed. At ID (near $x = 1.60$ m in Fig. 6), the skewness is driven by a positive peak from the low-pass filtered fluctuations, for both medium and large TSBs, that seems proportional in amplitude with the length of recirculation (Le Floc'h *et al.*, 2020). However, it is not the case for the small TSB, offering a distinction between *attached* and *separated* flows. A second remarkable feature comes from the kurtosis distributions. If all three TSBs show the same collapse of high frequency at the onset of separation in Fig. 7, a clear discrepancy between the large TSB versus the two smaller cases appears as the low-pass filtered component visibly dominates over the band-pass one, suggesting that the breathing is the first contributor to the kurtosis ahead of the vortex shedding, whereas the opposite is observed for the medium and small TSBs.

Thus, both time domain criteria using filtered components allow us to draw distinct portraits of separated versus attached flows, as well as between weak and massive separations.

High-order Moments for the Three Databases

The skewness and kurtosis distributions of p_w associated with the large TSB and the two airfoils are presented in Fig. 8 and Fig. 9 respectively. The streamwise axes are scaled to better superimpose all three recirculation databases: the large TSB uses x/L_b with L_b the mean recirculation length, 0 and 1 refer to the mean separation and reattachment points respectively.

Only the last 40% of the chord are shown for the two airfoils, as both recirculations for the NACA 4418 and DU96-W-180 ($\alpha = 7.8°$) are defined between $x/c \simeq 0.8$ and the trailing edge. That way, the forward flow fraction distributions for the flat plate and the NACA 4418 (blue curves) are easily aligned. The three databases indicate the same pattern. However, the two airfoil databases do not capture the skewness and kurtosis
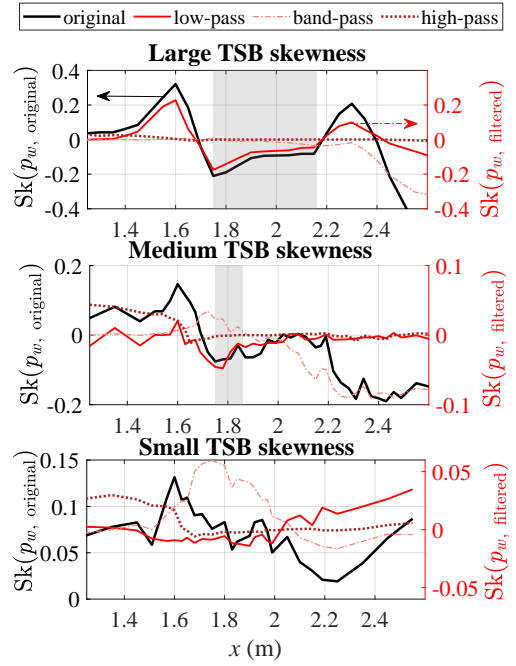

Figure 6: Large, medium and small TSB on a flat plate. Left y-axis: Skewness of p_w in black. Right y-axis: low-, band- and high-passed contributions in red.
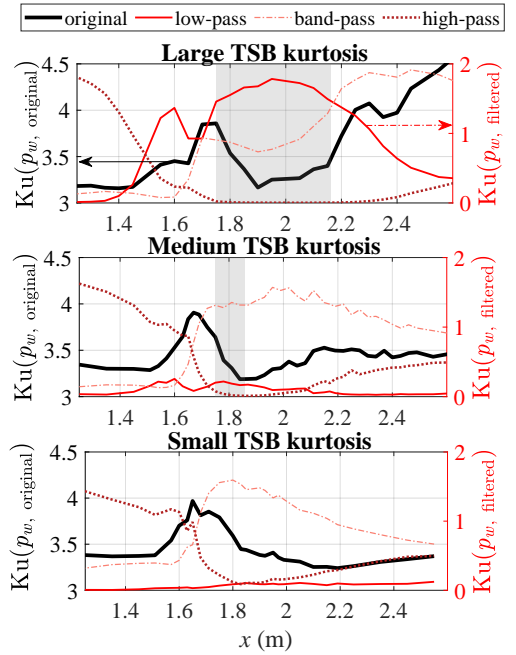

Figure 7: Large, medium and small TSB on a flat plate. Left y-axis: Kurtosis of p_w in black. Right y-axis: low-, band- and high-passed contributions in red.

peaks of the APG in Figs. 8 and 9, as the two airfoils focus is on the last 30% of the chord. Between the large TSB and the NACA 4418, low-pass results consistently showed a similar switch from positive near ID to negative skewed p_w inside the recirculation, and for these two massive separations, the breathing range dominate their kurtosis. Finally, DU96-W-180 shows an absence of low-pass activity as expected, and the band-pass results linked to the vortex shedding activity is the main driver for both high-order moments.
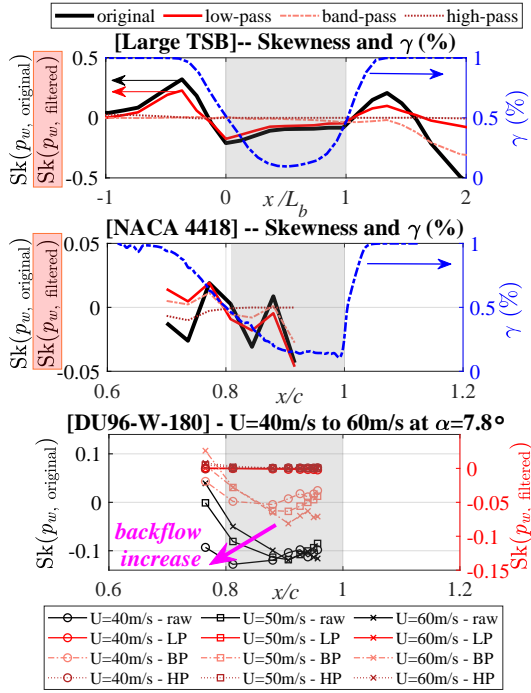
Figure 8: (Top) Large TSB and (Middle) NACA 4418: Left y-axis: Skewness of p_w in black, low-, band- and high-passed contributions in red. Right y-axis: Forward-flow fraction in blue. (Bottom) DU96-W-180: Left y-axis: Skewness of p_w in black. Right y-axis: low-, band- and high-passed contributions in red.

ferent airfoils in both time and frequency domains. The first conclusion is that both low ($St_L < 0.15$) and high ($St_L > 3$) frequency ranges can inform whether the boundary layer is separated or attached on the plate/airfoil surface. The illustration of backflow motion using the phase angle from the cross spectrum of two close wall pressure sensors enables a valuable diagnostic tool to rapidly detect the switch from a downstream classical vortex shedding to flow recirculation with an upstream motion. Secondly, time domain criteria such as the high-order moments of p_w further help to draw the portrait of a separated turbulent boundary layer. More specifically, the low-frequency range (when resolved) indicated that the regions upstream and downstream of separation can be used to distinguish between attached, weakly or massively separated conditions. Finally, further evaluation of each of these unsteady phenomena needs to be addressed for separation noise modeling. Indeed, the breathing motion, the vortex shedding, and the small scales involved in the recirculation and high-frequency turbulence likely contribute to the acoustic response of the scattered boundary layer pressure fluctuations at the trailing edge, though this interaction remains poorly understood.

REFERENCES

Bendat, Julius S & Piersol, Allan G 2011 *Random data: analysis and measurement procedures*, , vol. 729. John Wiley & Sons.

Byun, Gwibo & Simpson, Roger L 2010 Surface-pressure fluctuations from separated flow over an axisymmetric bump. *AIAA journal* **48** (10), 2397–2405.

Gibeau, Bradley & Ghaemi, Sina 2021 Low-and mid-frequency wall-pressure sources in a turbulent boundary layer. *Journal of Fluid Mechanics* **918**, A18.

Le Floc'h, A. 2021 Étude expérimentale d'une famille de bulbes de décollement turbulents. PhD thesis, École de technologie supérieure.

Le Floc'h, A., Weiss, J., Mohammed-Taifour, A. & Dufresne, L. 2020 Measurements of pressure and velocity fluctuations in a family of turbulent separation bubbles. *Journal of Fluid Mechanics* **902**, A13.

Ma, A., Gibeau, B. & Ghaemi, S. 2020 Time-resolved topology of turbulent boundary layer separation over the trailing edge of an airfoil. *Journal of Fluid Mechanics* **891**, A1.

Mohammed-Taifour, A. & Weiss, J. 2016 Unsteadiness in a large turbulent separation bubble. *Journal of Fluid Mechanics* **799**, 383–412.

Naka, Yoshitsugu, Stanislas, Michel, Foucaut, Jean-Marc, Coudert, Sebastien, Laval, Jean-Philippe & Obi, Shinnosuke 2015 Space-time pressure-velocity correlations in a turbulent boundary layer. *Journal of Fluid Mechanics* **771**, 624.

Sasaki, Kyuro & Kiya, Masaru 1985 Effect of free-stream turbulence on turbulent properties of a separation-reattachment flow. *Bulletin of JSME* **28** (238), 610–616.

Suryadi, A. 2019 Kinematic and acoustic similarities of separated turbulent boundary layers. *AIAA Journal* **57** (6), 2435–2446.

Suryadi, A. & Herr, M. 2015 Wall pressure spectra on a DU96-W-180 profile from low to pre-stall angles of attack. In *21st AIAA/CEAS Aeroacoustics Conference*.

Wang, S. & Ghaemi, S. 2022 Unsteady motions in the turbulent separation bubble of a two-dimensional wing. *Journal of Fluid Mechanics* **948**, A3.
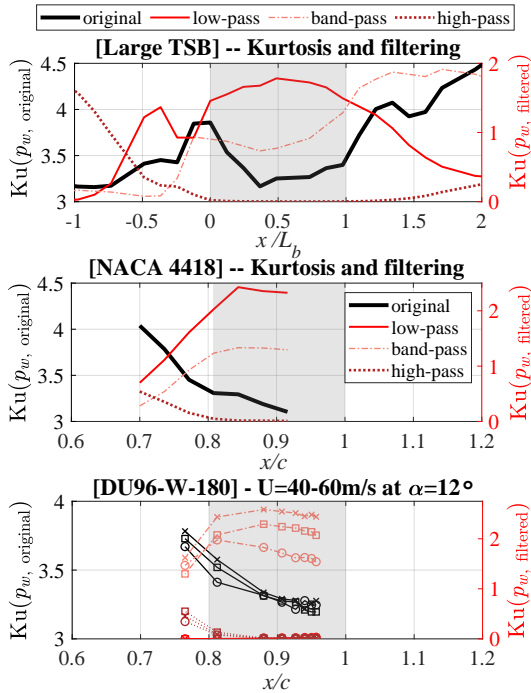

Figure 9: (Top) Large TSB, (Middle) NACA 4418 and (Bottom) DU96-W-180. Left y-axis: Kurtosis of p_W in black, Right y-axis: low-, band- and high-passed contributions in red.

CONCLUSION

Investigating flow separation using multiple databases revealed promising analogies between the flat plate and two dif-